THE ASTROPHYSICAL JOURNAL, 422:570–585, 1994 February 20

THE MULTIFREQUENCY SPECTRAL EVOLUTION OF BLAZAR 3C 345 DURING THE 1991 OUTBURST

J. R. WEBB,[1] C. R. SHRADER,[2] T. J. BALONEK,[3] D. M. CRENSHAW,[4] D. KAZANAS,[2] S. CLEMENTS,[5] A. G. SMITH,[5]
A. D. NAIR,[5] R. J. LEACOCK,[5] P. P. GOMBOLA,[5] A. SADUN,[6] H. R. MILLER,[7] I. ROBSON,[8] R. FUJIMOTO,[9]
F. MAKINO,[9] T. KII,[9] H. ALLER,[10] M. ALLER,[10] P. HUGHES,[10] E. VALTAOJA,[11] H. TERÄSRANTA,[11]
E. SALONEN,[11] M. TORNIKOSKI,[11] AND W. CHISM[1]

Received 1993 July 28; accepted 1993 August 30

ABSTRACT

The blazar 3C 345 underwent a 2.5 mag optical outburst between 1990 November and 1991 May. We have obtained 10 nearly simultaneous multifrequency spectra during the course of the outburst in order to study the multifrequency spectral variations of 3C 345 as a function of time. Although our observations were not sampled frequently enough to completely resolve the variations in every frequency band, the general rise and decline of the outburst were seen in the UV through radio with differing rise times. Simulations of an electron distribution injected into a tangled magnetic field show a relationship between frequency and characteristic timescale that was also observed in the radio variations of 3C 345. The two X-ray observations made during the monitoring period showed no evidence of variability. The multifrequency spectrum was modeled with two major components: a relativistic jet and a relativistic thermal accretion disk. Models calculated for each spectrum indicate that the outburst can be explained in terms of these models by varying the high-energy cutoff of the injected electron distribution in the jet model, while also varying the mass accretion rate in the disk model. There is marginal evidence that the inferred accretion rate varies with the jet luminosity.

Subject headings: quasars: individual (3C 345) — radio continuum: galaxies — ultraviolet: galaxies — X-rays: galaxies

1. INTRODUCTION

The blazar 3C 345 ($z = 0.595$; Burbidge 1965) has a long history of optical variations (Smyth & Wolstencroft 1970; Webb et al. 1988) and exhibits a high degree of variable polarization (Smith et al. 1986). Radio flux monitoring has shown that large-amplitude variations are common in that frequency range as well (Aller et al. 1985). In addition, superluminal radio components have been observed in 3C 345 (Kollgaard, Wardle, & Roberts 1989) which appear to be correlated with the radio flux variations. The general multifrequency spectrum of this source was studied by Bregman et al. (1986) and the variability of the radio to UV continuum was investigated by Brown et al. (1989). The previous studies found that the spectrum exhibits a "blue bump" in the optical-UV region and that the optical and IR spectral slope varies between -1.5 and -1.7.

Prior to our observations, 3C 345 had been in an extremely faint state with a B magnitude of approximately 18.1 in 1990 May (Kidger & Takalo 1990). In 1990 November, 3C 345 underwent an outburst brightening to nearly $B = 15.40$. Figure 1 shows the long-term light curve of 3C 345 with the 1991 outburst included. Except for some of the 1991 points, all of the observations in Figure 1 are photographic photometry from the University of Florida's Rosemary Hill Observatory (RHO). Although the present outburst was not the brightest ever recorded for 3C 345, its relatively rapid increase from a minimum state and its subsequent rapid decline are reminiscent of outbursts observed in this source during the early 1970s. The 1991 outburst was followed by a second outburst which occurred in early 1992 (Kidger et al. 1993).

The observations reported here were in a large part driven by an *International Ultraviolet Explorer* (*IUE*) Target of Opportunity (TOO) program designed to observe a quasar in outburst and to follow its evolution in the optical and UV. The TOO program focused on a small list of 15 optically violently variable (OVV) quasars and BL Lac objects which have shown large-amplitude optical flares during the years of monitoring at RHO. The monitoring frequency of the sources on this list were increased at RHO and at Colgate University's Foggy Bottom Observatory (FBO) in order to detect outbursts quickly. We activated the *IUE* TOO program based on observations of 3C 345 reported by Borgeest & Schramm (1991) and on follow-up photometry from RHO and FBO. The optical monitoring at RHO and FBO of 3C 345 was further increased to utilize every available clear night during the outburst. The X-ray observations were obtained by three of us (R. F., F. M., and T. K.) as part of a program of *Ginga* active galactic nucleus (AGN) observations. The radio, millimeter, IR, and supplementary optical observations were obtained under separate AGN monitoring programs and combined with our optical and UV data to form a comprehensive picture of 3C 345 during this period of activity.

---

[1] Department of Physics, Florida International University, Miami, FL 33199.

[2] Code 668.1, NASA/Goddard Space Flight Center, Greenbelt, MD 20771.

[3] Department of Physics and Astronomy, Colgate University, 13 Oak Drive, Hamilton, NY 13346-1396.

[4] Code 684.9, NASA/Goddard Space Flight Center, Greenbelt, MD 20771.

[5] Department of Astronomy, 211 SSRB, University of Florida, Gainesville, FL 32611.

[6] Bradley Observatory, Agnes Scott College, Decatur, GA 30030.

[7] Department of Physics, Georgia State University, Atlanta GA 30303.

[8] UKIRT, 660 North A'ohoku Place, University Park, Hilo, HI 96720.

[9] Institute for Space and Astronautical Science, 3-1-1, Yoshinodai, Sagamihara, Kanagawa 229, Japan.

[10] Astronomy Department, 817 Dennison Building, University of Michigan, Ann Arbor, MI 48109-1090.

[11] Metsähovi Radio Research Station, SF-02540 Kylmälä, Finland.

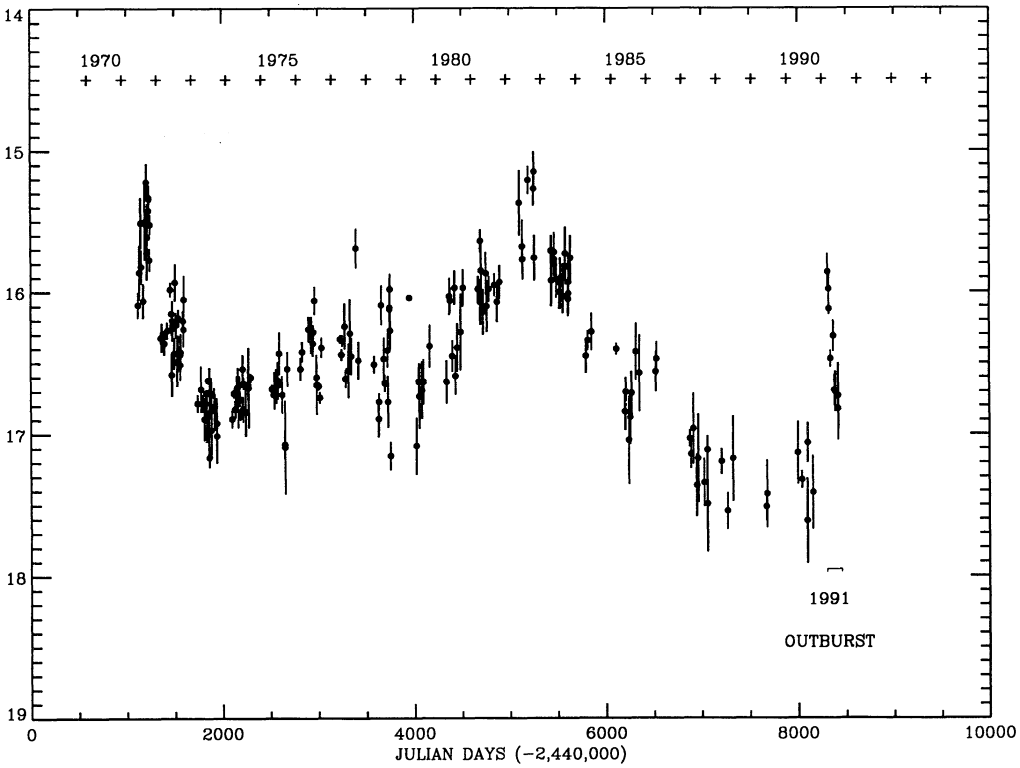

FIG. 1.—Long-term *B*-band curve of 3C 345 from Rosemary Hill Observatory. The plus signs along the top indicate the first day of each year. The duration of the 1991 outburst is indicated by the bracket below the light curve.

2. OBSERVATIONS

In this section, we give a brief description of the observations in decreasing frequency order. References to data collection and analysis procedures in each frequency band are made where appropriate. A log of all of the observations is presented in Table 1. Column (1) lists the modified Julian Date, column (2) the civil date, column (3) the observatory, and column (4) the bandpass.

2.1. *X-Ray*

The X-ray observations of 3C 345 were obtained on 1991 April 6.3–6.5 UT, May 25.2–25.8 UT, and May 27.2–27.8 UT, with the large-area counter (LAC) array on *Ginga* (Turner et al. 1989). The April 6.3–6.5 (UT) observation was fitted to a simple model consisting of a power law and a low-energy exponential absorption component, which yielded a photon index of 1.54 ± 0.02 and a normalization of 2.03×10^{-3} photons $\mathrm{s^{-1}\,cm^{-2}\,keV^{-1}}$ at 1 keV. The May 25.2–25.8 and May 27.2–27.6 observations yielded photon indices of 1.58 ± 0.05 and 1.46 ± 0.23, and normalizations of 1.86×10^{-3} and 1.27×10^{-3} between 1.16 keV and 23.16 keV. The individual May observations were combined; the weighted average of the photon index was 1.53 ± 0.05, and the normalization was 1.589×10^{-3}. The hydrogen column density was fixed at $1.0 \times 10^{20}\ \mathrm{cm^{-2}}$ for each observation, since the LAC in insensitive to column densities below $5 \times 10^{20}\ \mathrm{cm^{-2}}$ and since previous estimations of the column density toward 3C 345 made with *Einstein* imaging proportional counter (IPC) observations (Webb 1988) also agree with Galactic column densities of around $1 \times 10^{20}\ \mathrm{cm^{-2}}$. These values for N_{H} are each consistent to within a nominal factor of 2 of the value obtained by applying an empirical scaling factor to the color excess $E(B-V) = 0.01$.

2.2. *Ultraviolet*

Ultraviolet observations were obtained with the *International Ultraviolet Explorer* (*IUE*) throughout the decline of the outburst. During a 200 day period, we obtained 12 good-quality low-dispersion spectra (six SWP and six LWP). The spectra were systematically reduced using the *IUE* RDAF Gaussian extraction routine (GEX). The most prominent features visible in the UV spectrum are the redshifted Lyman-α (1946 Å) and the C IV line at 2470 Å. The poor signal-to-noise ratio, especially in the SWP, and the presence of camera artifacts and reseaux prevent firm identification of other lines. The identification of Lyman-β + O III in the 1620 Å region by Bregman et al. (1986) is questionable, since there is a strong artifact in this region (Crenshaw, Bruegman, & Norman 1990). Weak C III] emission at 3000 Å may be present, but unfortunately it falls near a reseau and is thus partially obliterated. The ratio of the C IV/Lyman-α lines is nearly unity. The UV spectra are too noisy to detect emission-line variations at levels less than a factor of 3.

To analyze the continuum variations, each individual spectrum was corrected for effects of cosmic-ray hits and reseaux by linear interpolation between adjacent continuum regions and smoothed using a five-point boxcar. The SWP spectra were binned around 1600 Å with a bin width of 600 Å. The LWP binning was done at 2800 Å with a bin width of 400 Å.

Figure 2 shows the UV long-term light curve at 1600 and 2800 Å. The 4400 Å (*B* band) light curve is also shown for comparison. The correlation between the frequency bands is apparent, although the UV points are sparsely sampled. The

TABLE 1

LOG OF OBSERVATIONS

MJD (1)	Date (2)	Observatory (3)	Bandpass (4)
8005......	1990 Apr 23	UKIRT	*J*, *H*, *K*, *L*
8008......	1990 Apr 26	Univ. Michigan	4.8, 8 GHz
8008......	1990 Apr 26	Metsāhovi	14.5, 22, 37 GHz
8310......	1991 Apr 22	RHO, FBO	*B*, *V*, *R*
8315......	1991 Feb 27	Metsāhovi	22, 37 GHz
8315......	1991 Feb 27	*IUE*	1975–3300 Å
8316......	1991 Feb 28	Univ. Michigan	4.8 GHz
8316......	1991 Feb 28	*IUE*	1175–2000 Å
8321......	1991 Mar 05	Metsāhovi	14.5 GHz
8321......	1991 Mar 05	UKIRT	*J*, *H*, *K*, *L*
8322......	1991 Mar 06	Univ. Michigan	8 GHz
8325......	1991 Mar 09	Metsāhovi	22 GHz
8326......	1991 Mar 10	RHO, FBO	*B*, *V*, *R*
8326......	1991 Mar 10	*IUE*	1975–3300 Å
8339......	1991 Mar 23	*IUE*	1175–3300 Å
8342......	1991 Mar 26	Metsāhovi	37 GHz
8342......	1991 Mar 26	RHO, FBO	*U*, *B*, *V*, *R*
8349......	1991 Apr 02	Univ. Michigan	4.8 GHz
8351......	1991 Apr 04	FBO	*R*
8353......	1991 Apr 06	Metsāhovi	14.5 GHz
8353......	1991 Apr 06	*Ginga*	1–20 keV
8354......	1991 Apr 07	Mestāhovi	22, 37 GHz
8354......	1991 Apr 07	*IUE*	1175–3300 Å
8354......	1991 Apr 07	*IUE*	1175–3300 Å
8366......	1991 Apr 19	UKIRT	*J*, *H*, *K*, *L*
8367......	1991 Apr 20	Univ. Michigan	4.8 GHz
8367......	1991 Apr 20	NRAO	2 mm
8367......	1991 Apr 20	UKIRT	0.8, 1.1, 1.3 mm
8369......	1991 Apr 22	Mestāhovi	37 GHz
8369......	1991 Apr 22	RHO, FBO	*U*, *B*, *V*
8369......	1991 Apr 22	*IUE*	1175–3300 Å
8370......	1991 Apr 23	Metsāhovi	14.5, 22 GHz
8371......	1992 Apr 24	*IUE*	1975–3300 Å
8393......	1991 May 16	Univ. Michigan	8 GHz
8393......	1991 May 16	Metsāhovi	22, 37 GHz
8397......	1991 May 20	Univ. Michigan	4.8 GHz
8397......	1991 May 20	Metsāhovi	14.5 GHz
8400......	1991 May 23	UKIRT	*I*
8400......	1991 May 23	RHO, FBO	*B*, *V*, *R*
8402......	1991 May 25	*Ginga*	1–20 keV
8404......	1991 May 27	UKIRT	*I*
8405......	1991 May 28	Univ. Michigan	4.8 GHz
8405......	1991 May 28	Metsāhovi	37 GHz
8405......	1991 May 28	RHO, FBO	*V*, *R*
8405......	1991 May 28	*IUE*	1975–3300 Å
8406......	1991 May 29	Metsāhovi	14.5, 22 GHz
8410......	1991 Jun 02	Univ. Michigan	8 GHz
8414......	1991 Jun 06	*IUE*	1175–2000 Å
8417......	1991 Jun 09	Metsāhovi	22, 37 GHz
8417......	1991 Jun 09	NRAO	2 mm
8417......	1991 Jun 09	UKIRT	0.8, 1.1, 1.3 mm
8417......	1991 Jun 09	RHO	*B*
8418......	1991 Jun 10	UKIRT	450 μm
8424......	1991 Jun 16	UKIRT	*J*, *H*, *K*, *L*
8447......	1991 Jul 09	Metsāhovi	37 GHz
8447......	1991 Jul 09	UKIRT	*J*, *H*, *K*, *L*
8447......	1991 Jul 09	UKIRT	*J*, *H*, *K*, *L*
8455......	1991 Jul 17	NRAO	2 mm
8455......	1991 Jul 17	UKIRT	0.8, 1.1, 1.3 mm

first two panels of Figure 3 show the *IUE* UV observations made during the 1991 outburst. Figure 3 also shows the correspondence between the UV data and the *B* optical variations. The discrepant 1600 Å (SWP) point which shows an increase in flux on 1991 March 23 (JD 2,448,338) is suspect because the signal-to-noise ratio in that observation was extremely low, and because a corresponding increase in brightness was not seen in the LWP camera. The *IUE* spectra are consistent with no variations in the UV line strengths throughout the decline of the outburst.

2.3. *Optical*

The optical data include 27 *R*-band CCD measurements from FBO and a large number of *UBV* photographic measurements from RHO. The RHO data were reduced as described in Webb et al. (1988). Additional CCD *UBVRI* observations were obtained with the 24 inch (0.6 m) telescope at Capilla Peak Observatory and the 1.9 m at Kitt Peak Observatory. The *U*-, *B*-, *V*-, *R*-, and *I*-band observations are plotted in individual panels of Figure 3. All magnitudes are dereddened following Seaton (1979), using a color excess of $E(B-V) = 0.01$ (Hewitt & Burbidge 1987). A comparison of the light curves shows that the outburst decline occurred concurrently in all seven frequency bands, although the entire UV-optical-IR region was well sampled for only four epochs during the flare decline.

2.4. *Infrared-Millimeter*

The IR data were obtained as part of an ongoing blazar monitoring program at the UKIRT. This program regularly observes a number of blazar sources with the UKIRT telescope at Mauna Kea (Robson 1992). The IR and 0.8–2.0 mm data were obtained as part of a long-term monitoring program of blazars using the UKIRT and the James Clerk Maxwell Telescope (JCMT). The infrared data were obtained using the UKIRT service program and used standard techniques of measurement and calibration. The JCMT data were obtained using the continuum photometer (UKT14) and were calibrated using planets and secondary calibration sources as described in Duncan et al. (1990).

Observations made in the *J*, *H*, *K*, and *L*′ band (IR) are shown in Figure 4, while the flux variations at 800, 1100, and 1300 μm and 2 mm are plotted in Figure 5. The *J*, *H*, *K*, and *L*′ bands showed a marked decrease in flux during the later phases of the optical outburst, followed by a small brightening. The 800, 1100, and 1300 μm fluxes showed a large increase corresponding to the outburst that was followed by a small dip in the flux curve. The variations are smoother at longer wavelengths, although the sparse sampling prevented clear timescales to be attributed to the flare rise. The 2 mm data also show a high flux level after the 1991 optical outburst, but no short timescale variations are seen in the flux curve.

2.5. *Radio*

Radio observations from the University of Michigan's 26 m telescope were obtained at frequencies of 4.8, 8.0, and 14.5 GHz. Additional radio observations at 22 and 37 GHz were obtained at the Metsāhovi radio observatory in Finland (Teräsranta et al. 1992). The radio flux curves are shown in Figure 6. It is worth pointing out that at frequencies 14.5, 22, and 37 GHz an upward light-curve inflection occurs nearly simultaneously with the onset of the optical flare. A similar upward inflection is seen at lower frequencies, 8 and 4.8 GHz, but at a later time, suggesting that the low-frequency emission emanates at larger distances from the central source than the higher frequency emission. An increase in flux at 8 GHz occurs approximately 200 days after the corresponding increase at 22 GHz, and the increase at 4.8 GHz approximately 200 days after the 8 GHz flux begins to increase (Aller 1993).

2.6. *Multifrequency Spectra*

The data described in the previous sections have allowed us to construct 10 multifrequency spectra spanning at ∼5 month baseline. The *R*-band light curve is plotted in Figure 7 with

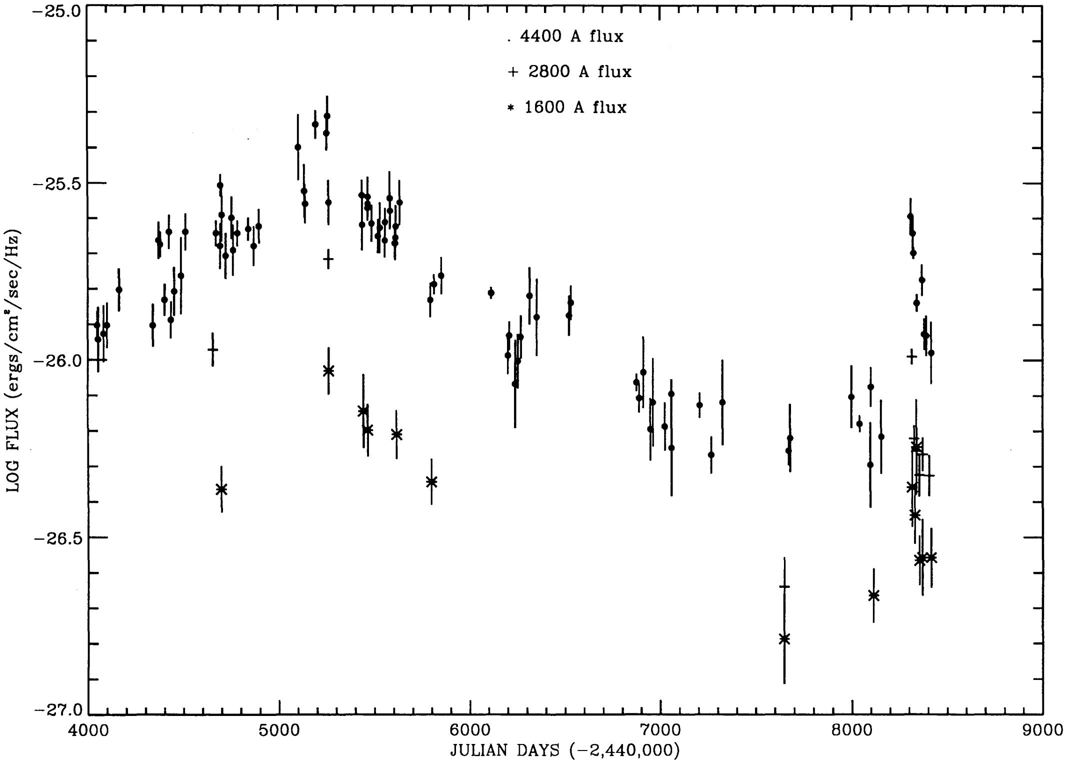

FIG. 2.—Long-term UV and optical flux curves are plotted including all available archival *IUE* data of 3C 345 and the RHO *B*-band observations. The *B* fluxes are plotted as dots, the LWP fluxes centered on 2800 Å plotted as plus signs, and the SWP fluxes centered on 1600 Å are represented by asterisks. This figure illustrates the correspondence between the optical flux variations and UV flux variations from about 1979 to the present outburst.

plus signs along the bottom to indicate the approximate epochs at which these multifrequency spectra were compiled. The spectra were constructed from observations made over as short a time interval as possible (5–10 days), to maximize the frequency coverage while minimizing possible effects of short-timescale variability. Although 5 and 10 day bins are small compared with many previously published multifreqency spectra, significant variations do take place in some frequency bands within these time periods, thus introducing an additional element of uncertainty into our analysis.

We present the individual multifrequency spectra in Figure 8. We have labeled the individual spectra "sp1" through "sp10." Table 2 is a compilation of the data that make up these spectra. The first row gives the spectrum identification (sp1, etc.), while the second row indicates the date of the center around which all of the observations are clustered. The third row gives the half-width of the bin in days, and successive rows indicate the frequency bands in which data are collected and identified in column (1). The data are given as flux and 1 σ errors and are in units of ergs cm^{-2} s^{-1} Hz^{-1}. Two additional multifrequency spectra from Bregman et al. (1986) were analyzed along with the 10 spectra from this study. These additional multifrequency spectra will be referred to as "sp81" and "sp83." A reference spectrum was created by adding these last two well-sampled spectra (sp81 and sp83); we consider this procedure reasonable because the brightness of 3C 345 was roughly constant during the 1981 and 1983 observations. The evolution of the multifrequency spectrum during the 1991 outburst is illustrated in the succession of frames in Figure 8. The reference spectrum is plotted as small dots in each frame. The first spectrum, sp1, was obtained prior to the outburst, while the other nine were made during the decline phase of the outburst.

Most of our data are consistent with a frequency-independent brightening of the source, the exception being the 8 and 4.8 GHz fluxes. In particular, the onset of the increase in the flux at 14, 22, and 37 GHz occurs almost simultaneously with the onset of the optical flare. Although our millimeter and IR data do not cover this epoch, they are consistent with the onset of flaring having occurred during the same time interval. The fluxes at 8 and 4.8 GHz, while not varying synchronously with higher frequency emissions, do exhibit an increase which is readily interpreted and a delayed response to the primary flare. This behavior could be attributed to self-absorption at low frequencies, or could be indicative of origination at larger distances from the QSO central engine than the bulk of the emission.

Examination of Figure 8 shows that the broad-band energy distribution derived from our observations has a slightly lower intensity and has a steeper IR-UV continuum than the reference spectrum. The radio flux levels are similar to those of the reference spectrum.

3. ANALYSIS AND MODELING

The data collected during this outburst are ideal for testing present theoretical models. Fitting homogeneous synchrotron–self-Compton (SSC) models (Urry 1984) to the data produced poor fits and unacceptably large Doppler factors (~100–150). In § 3.1 we examine the radio variability in detail, and in § 3.2 the entire multifrequency spectral distribution is considered.

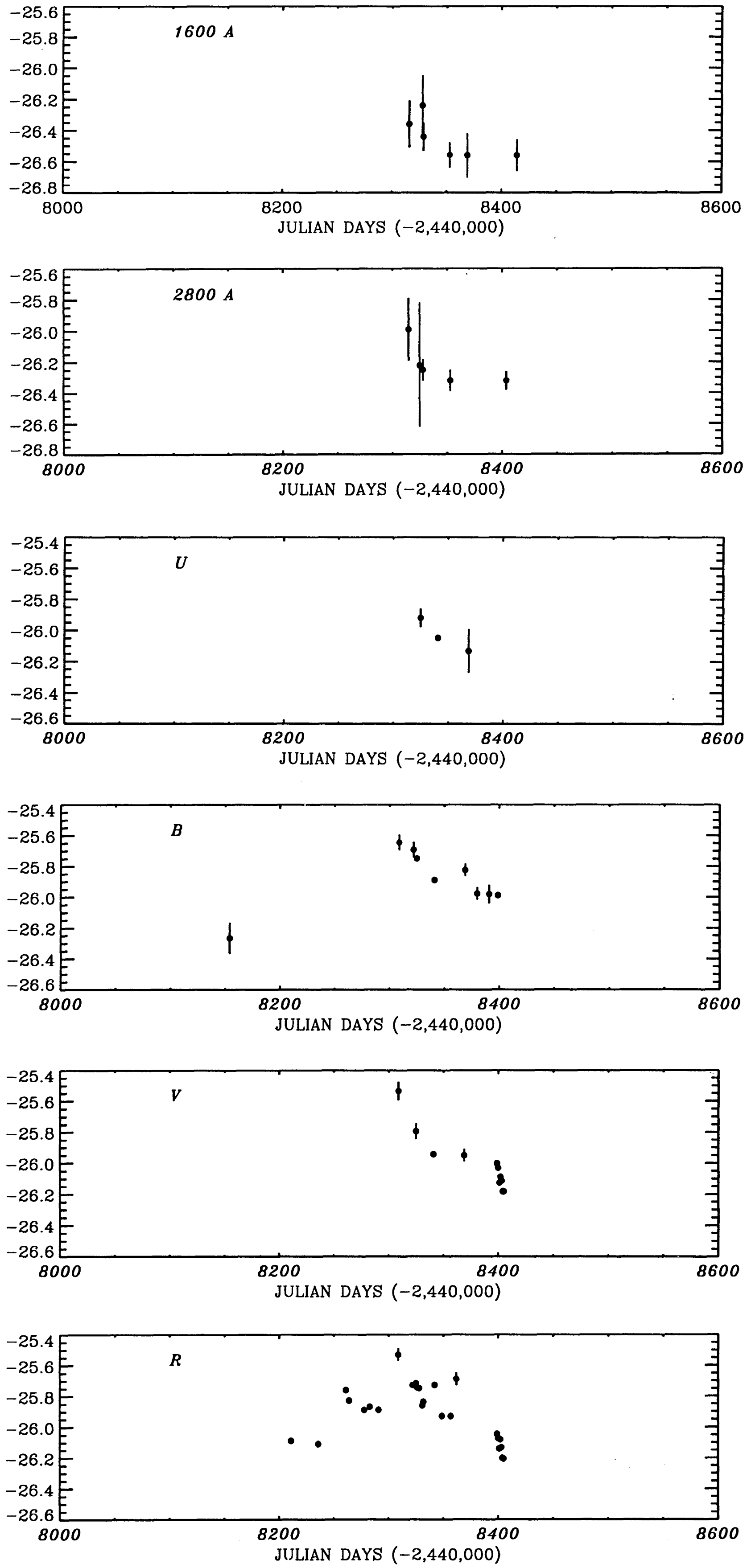

FIG. 3.—Individual UV (*first two panels*) *U*, *B*, *V*, *R*, and *I* flux curves of 3C 345 during the decline of the 1991 outburst. The horizontal and vertical scales are the same in each frame, showing the relative activity in each band.

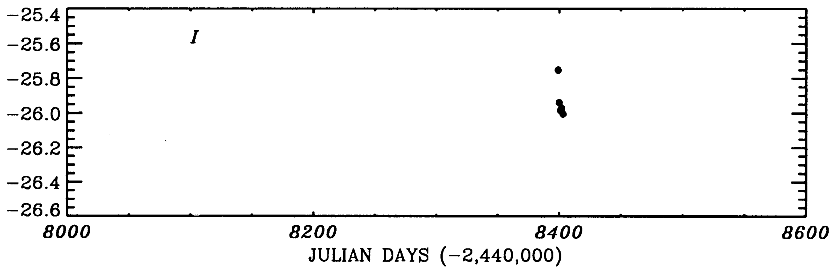

FIG. 3—*Continued*

3.1. *Variability Modeling*

The observed radio variations were compared with a simple model which follows the time evolution of the relativistic electron distribution under conditions of continuous electron injection, initiated at $t = 0$, in a volume of a given constant magnetic field. The resulting time-dependent synchrotron emission was computed by folding the electron distribution with the synchrotron emissivity in the δ-function approximation. At $t = 0$ the electron distribution function was assumed to be a power law given by $N_e(\gamma) = K_e \gamma^{-p}$ cm^{-3} ergs^{-1}, while starting at $t = 0$ a new population of electrons was continuously injected with a power-law distribution of the form $Q_e(\gamma) = q\gamma^{-\Gamma}$ cm^{-3} s^{-1} ergs^{-1}, where $\Gamma = p - 1$ ($\Gamma = 2$ in our simulations). The relationship between the indices of the injected and steady state electron distribution functions was established so that after synchrotron losses the newly injected electrons developed a nonthermal power-law distribution with spectral index identical to that of the electrons initially present in the given volume. As a result of these freshly injected electrons, the steady electron distribution function at each energy underwent an increase in amplitude. The change in amplitude was the same for all electron energies because of the particular choice of indices Γ and p; however, the timescale for reaching the new equilibrium was different for the different electron energies owing to the energy-dependent character of synchrotron losses [$d\gamma/dt = b\gamma^2$ and $b \cong (4/3)\sigma_T c(B^2/8\pi)$]. When the injected particles energies were folded through the synchrotron emissivity, a different characteristic relaxation timescale was obtained for the resulting synchrotron emission in different frequency bands. Under the conditions of continuous electron injection and assuming the form of the electron spectrum at $t = 0$, the time-dependent electron distribution function is obtained by solving the electron kinetic equation. For $bt\gamma < 1$, the distribution function is

$$N_e(\gamma, t) = K_e \gamma^{-p}(1 - bt\gamma)^{p-2} + \frac{q\gamma^{-(p+1)}}{b(\Gamma - 1)} [1 - (1 - bt\gamma)^{\Gamma - 1}] .$$

The distribution function is zero if $bt\gamma > 1$ by definition.

When folded with the synchrotron emissivity, which can be approximated by the δ-function $\epsilon(\nu, \nu_c) \propto \delta(\nu - \gamma^2 \nu_c)$, the above electron distribution function yields the synchrotron emission at each frequency ν, where $\nu_c = 4 \times 10^6 B$ Hz is the cyclotron frequency and B is in gauss. Because an electron of

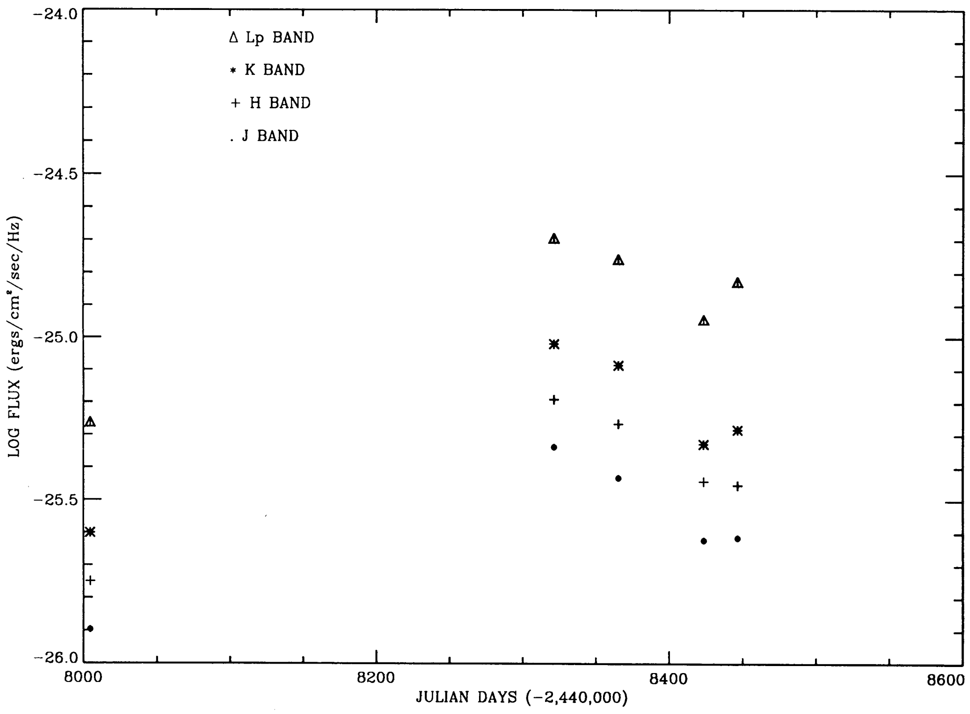

FIG. 4.—Same as Fig. 3, but for J, H, K, and L' bands. The gap between 8000 and 8300 days prevents a determination of the rise time of the flare in those bands.

1994ApJ...422..570W

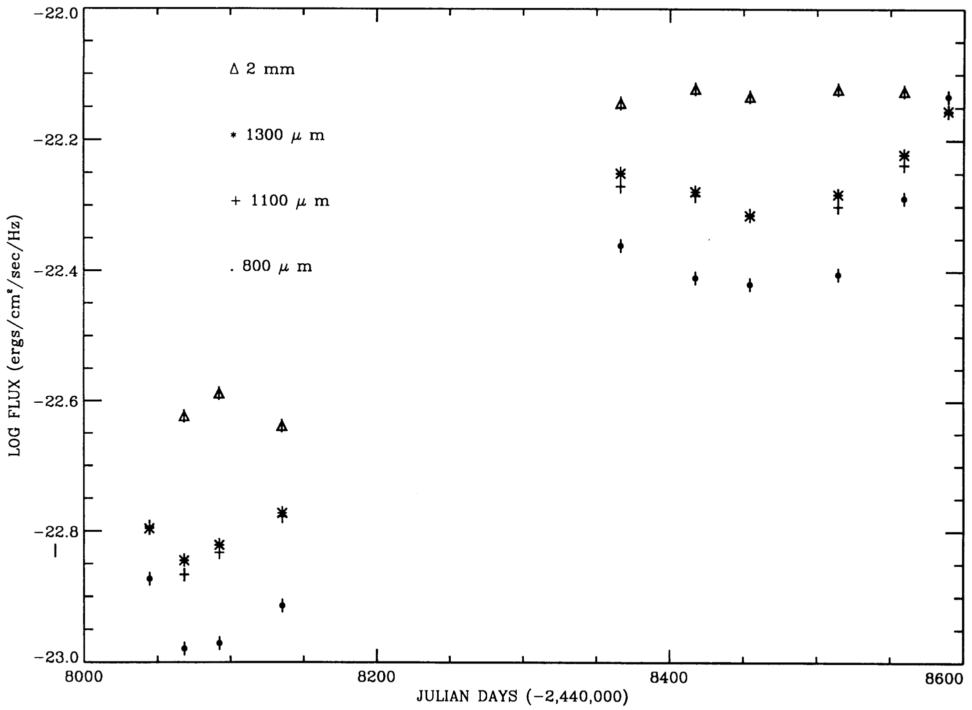

FIG. 5.—Same as Fig. 3, but for 800, 1100, 1300 μm and 2 mm bands. Again, the gap between 8140 and 8350 days allows only a lower limit estimate of a rise time.

Lorentz factor γ emits most of its energy at frequency $\gamma^2 \nu_c$ and because the characteristic timescale for synchrotron losses are proportional to γ^{-1}, one would expect in the context of this simple model that the variability timescale for each frequency would be inversely proportional to the square root of the frequency, i.e., $\tau(\nu) \propto \nu^{-1/2}$ (see also Marscher & Gear 1985). The numerical modeling results fit this scaling law very well.

The variability timescale for each radio-frequency band observed was estimated by fitting an exponential to the rising segment of the light curves. Unfortunately, our temporal coverage undersamples frequencies greater than 50 GHz (with the exception of optical frequencies). As a result, the variability timescales we obtain represent only upper limits to the real timescales. In the 2 mm and the 1300, 1100, and 1300 μm data,

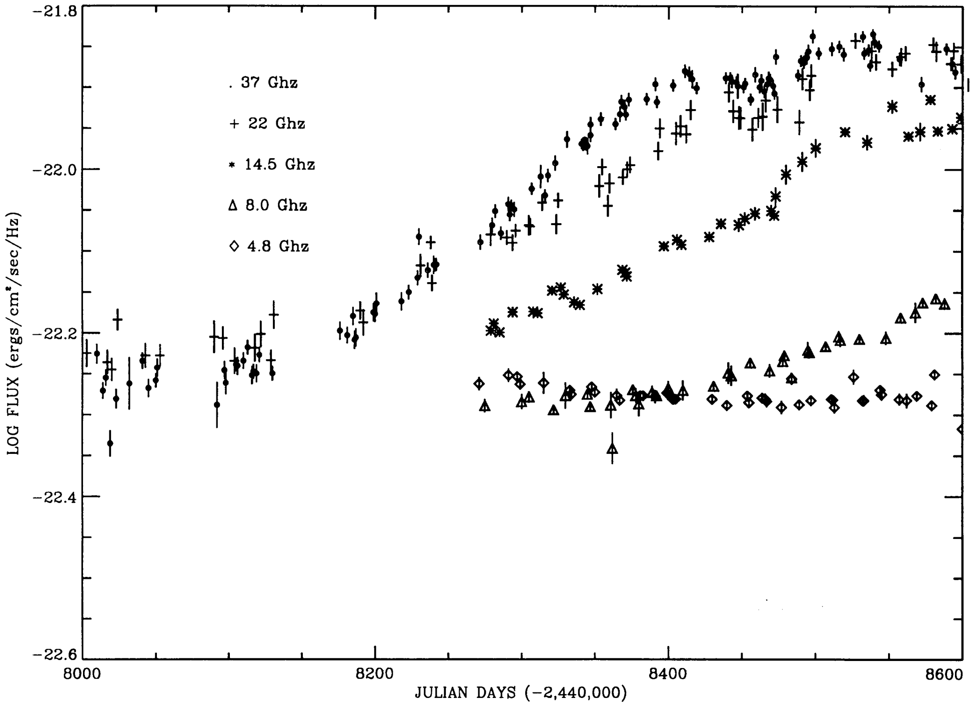

FIG. 6.—Same as Fig. 3, but for 37, 22, 14.5, 8.0, and 4.8 GHz data. The sampling in these bands allows an accurate determination of the rise times, and they are compared with theoretical models in § 3.1.

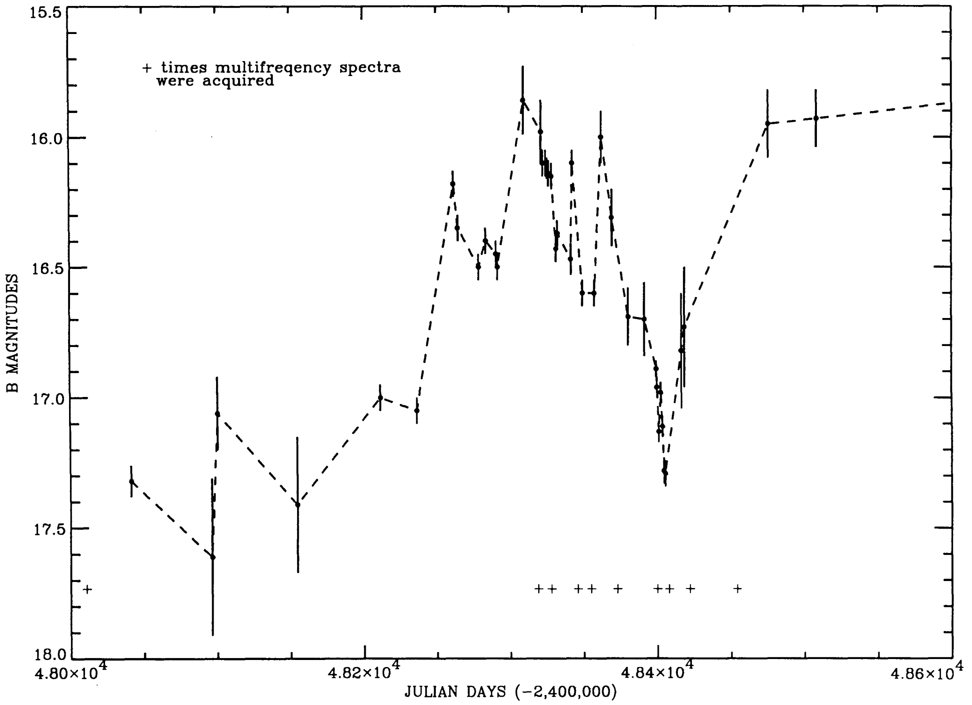

FIG. 7.—*B*-band light curve of 3C 345 during the 1991 outburst. The plus signs along the bottom of the plot indicate the approximate times when multifrequency spectra were compiled. The dashed line is intended merely to show the temporal order of the observations. The last two points are included to show a secondary outburst that occurred after our program has finished.

there are large gaps which provide only upper limits on the variability timescales at those frequencies, but there is an indication that these timescales tend to decrease toward higher frequencies also. We have calculated the relationship between the rise time and frequency from the 4.8, 8, 14, 22, and 37 GHz data and have plotted their logarithms in Figure 9. It is apparent that the relation obtained from these observations is in qualitative agreement with that expected within our simple model. Considering the simplifications in this model (uniform magnetic field, etc.), it is rather surprising that there is such good agreement with the data. Extrapolating the relationship thus obtained from the radio observations to the optical (using the scaling quoted before) yields a timescale of the order of 10 days for the optical frequencies, a value consistent with some of the more rapid variations seen in the *R*-band optical data.

3.2. *Multifrequency Spectra Models*

In view of the success of the simple injection model, an effort was made to model the entire multifrequency spectrum in terms of an SSC model. Linear fits over restricted frequency ranges were made in order to determine the behavior of each part of the spectrum during the outburst. In the optical-IR region, the fits were subtracted from the IR-optical power-law component to obtain possible blue-bump components. If a discernible nonlinearity was present, we fitted a baseline to the data in that region instead of using a least-squares "best-fit" line to the data. The power laws obtained in the IR-optical-UV portion of the spectrum ranged from -1.27 to -2.7, with a mean of -1.58. Spectral indices derived in a similar fashion using the Bregman et al. (1986) multifrequency data give spectral slopes of -1.56 ± 0.26 for the 1981 spectrum and -1.49 ± 0.07 for the 1983 spectrum. Brown et al. (1989) found the optical spectral index of 3C 345 to be between -1.05 and -1.74 with a mean of -1.5, consistent with our observations. Although the statistics are poor, there seems to be no correlation of the spectral index with either flux level or time as the outburst progressed after subtraction of the blue-bump component. A comparison of the "best-fit" slopes (no bump component removed) yields essentially the same result. The complex multifrequency behavior exhibited by 3C 345 during the outburst decline suggests that more than one variable component is necessary in order to model the broad-band variability.

VLBI studies of 3C 345 indicate the presence of a jet in 3C 345 (Bartel et al. 1984; Tang, Rönnäng, & Bååth 1989). Bregman et al. (1986) and Sadun (1992) have found solid evidence for correlation between optical activity and superluminal components in radio jets of some quasars. Due to the plausibility of relativistic motion in this source, we chose to model the broad-band continuum of 3C 345 in terms of a synchrotron–self-Compton jet (Königl 1981; Hutter & Mufson 1986) and the blue-bump component as a thermal accretion disk.

The jet model assumes a power-law distribution of relativistic electrons, $N(\epsilon) = K_1(r/r_0)^n$, injected into a jet with opening half-angle ϕ, viewing angle θ, and no external pressure. The radius r is measured from the jet apex, and $r_0 = 1.0$ pc. The electrons expand into a tangled magnetic field whose strength varies as a function of distance from the central source $B = B_1(r/r_0)^m$. Continuous reacceleration along the jet is assumed in order to offset radiative losses.

One of the major problems with these types of jet models has been the large number of free parameters available to fit the data. Each individual model is poorly constrained by the observations, allowing the model to fit any spectrum. We have applied the model with the philosophy that once we obtain a fit

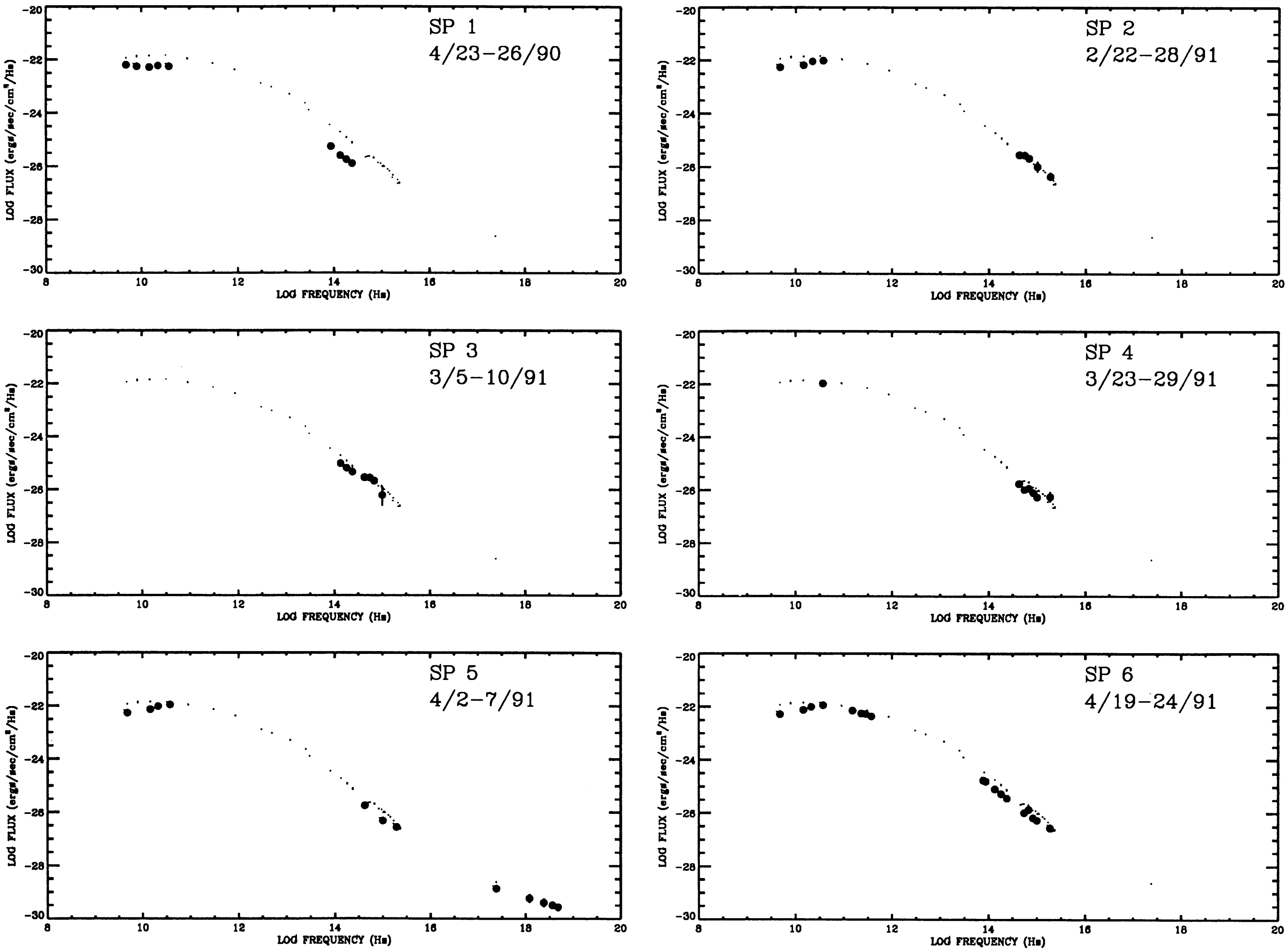

FIG. 8.—Multifrequency spectra throughout the 1991 outburst. The small dots represent the "reference spectrum" (see text), while the larger dots represent the observations at each epoch. Errors are smaller than symbol size unless explicitly shown.

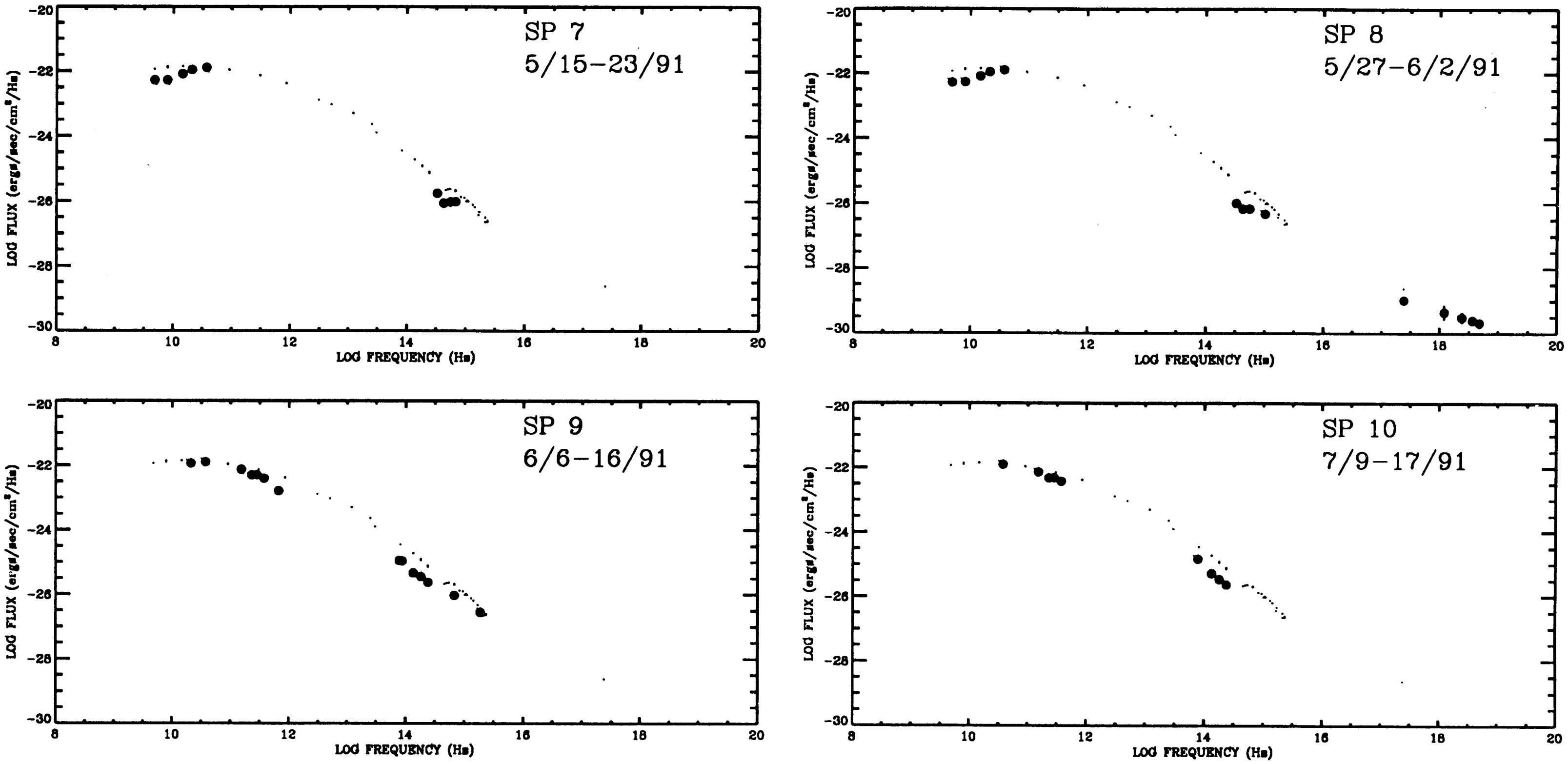

FIG. 8—*Continued*

TABLE 2

Data from Multifrequency Spectra

	Spectrum[a]																			
	sp1		sp2		sp3		sp4		sp5		sp6		sp7		sp8		sp9		sp10	
	1990 Apr 24.5		1991 Feb 25.0		1991 Mar 24.5		1991 Mar 7.5		1991 Apr 4.5		1991 Apr 21.0		1991 May 19.5		1991 May 29.0		1991 Jun 11.0		1991 Jul 13.0	
	1.5		3.0		1.5		2.5		2.0		2.5		3.5		4.0		5.0		4.0	
log ν	S[b]	dS[b]	S	dS	S	dS	S	dS	S	dS	S	dS	S	dS	S	dS	S	dS	S	dS
18.68	...	...	...	...	...	...	...	...	−29.570	0.140	...	...	...	...	−29.666	0.180	...	...	...	...
18.56	...	...	...	...	...	...	...	...	−29.493	0.140	...	...	...	...	−29.605	0.114	...	...	...	...
18.38	...	...	...	...	...	...	...	...	−29.401	0.160	...	...	...	...	−29.504	0.160	...	...	...	...
18.08	...	...	...	...	...	...	...	...	−29.240	0.168	...	...	...	...	−29.349	0.224	...	...	...	...
17.38	...	...	...	...	...	...	...	...	−28.870	0.070	...	...	...	...	−28.975	0.100	...	...	...	...
15.27	...	...	−26.357	0.150	...	...	−26.243	0.190	−26.564	0.080	−26.556	0.140	...	...	...	...	−26.556	0.100	...	...
15.00	...	...	−25.990	0.200	−26.219	0.400	−26.254	0.070	−26.322	0.070	−26.264	0.050	...	...	−26.324	0.060	...	...	...	...
14.92	...	...	...	...	...	...	−26.085	0.010	...	...	−26.169	0.140	...	...	...	...	...	...	...	...
14.83	...	...	−25.678	0.050	−25.678	0.050	−25.922	0.020	...	...	−25.858	0.040	−26.022	0.020	...	...	−26.026	0.010	...	...
14.74	...	...	−25.559	0.060	−25.559	0.060	−25.967	0.020	...	...	−25.975	0.040	−26.027	0.020	−26.167	0.020	...	...	...	...
14.63	...	...	−25.547	0.040	−25.547	0.040	−25.747	0.020	−25.747	0.020	...	...	−26.063	0.010	−26.172	0.020	...	...	...	...
14.52	...	...	...	...	...	...	...	...	...	...	...	...	−25.764	0.020	−26.000	0.020	...	...	...	...
14.38	−25.896	0.010	...	...	−25.336	0.010	...	...	...	...	−25.431	0.010	...	...	...	...	−25.622	0.010	−25.614	0.010
14.26	−25.750	0.010	...	...	−25.190	0.010	...	...	...	...	−25.265	0.010	...	...	...	...	−25.441	0.010	−25.454	0.010
14.13	−25.600	0.010	...	...	−25.019	0.010	...	...	...	...	−25.086	0.010	...	...	...	...	−25.327	0.010	−25.283	0.010
13.94	−25.261	0.010	...	...	...	...	...	...	...	...	−24.795	0.010	...	...	...	...	−24.956	0.010	...	...
13.89	...	...	...	...	−24.693	0.010	...	...	...	...	−24.757	0.010	...	...	...	...	−24.943	0.010	−24.826	0.010
11.82	...	...	...	...	...	...	...	...	...	...	...	...	...	...	...	...	−22.788	0.010	...	...
11.57	...	...	...	...	...	...	...	...	...	...	−22.361	0.010	...	...	...	...	−22.410	0.010	−22.420	0.010
11.45	...	...	...	...	...	...	...	...	...	...	−22.270	0.010	...	...	...	...	−22.284	0.010	−22.313	0.010
11.36	...	...	...	...	...	...	...	...	...	...	−22.250	0.010	...	...	...	...	−22.278	0.010	−22.314	0.010
11.18	...	...	...	...	...	...	...	...	...	...	−22.144	0.010	...	...	...	...	−22.122	0.010	−22.134	0.010
10.57	...	...	...	...	...	...	...	...	−21.959	0.008	−21.945	0.007	−21.896	0.008	−21.898	0.007	−21.890	0.010	−21.894	0.007
10.57	−22.250	0.009	−22.009	0.014	−21.993	0.009	−21.969	0.006	...	...	...	...	...	...	...	...	...	...	...	...
10.34	−22.225	0.017	−22.041	0.010	−22.067	0.012	...	...	...	...	...	...	...	...	...	...	...	...	...	...
10.32	...	...	...	...	...	...	...	...	−22.021	0.014	−22.010	0.009	−21.950	0.012	−21.956	0.014	−21.928	0.012	...	...
10.16	−22.286	0.006	−22.175	0.003	−22.148	0.004	...	...	−22.146	0.007	−22.124	0.003	−22.094	0.004	−22.090	0.005	...	...	...	...
9.90	−22.248	0.005	...	...	−22.294	0.006	...	...	...	...	...	...	−22.274	0.004	−22.270	0.012	...	...	...	...
9.68	−22.197	0.001	−22.261	0.013	...	...	...	...	−22.269	0.003	−22.280	0.005	−22.275	0.004	−22.281	0.002	...	...	...	...

[a] The first line identifies the spectrum, the second line gives the date (see text), and the third line gives the bin half-width in days.

[b] S = flux, $dS = 1\ \sigma$ error, in units of ergs $\mathrm{cm^{-2}\ s^{-1}\ Hz^{-1}}$.

1994ApJ...422..570W

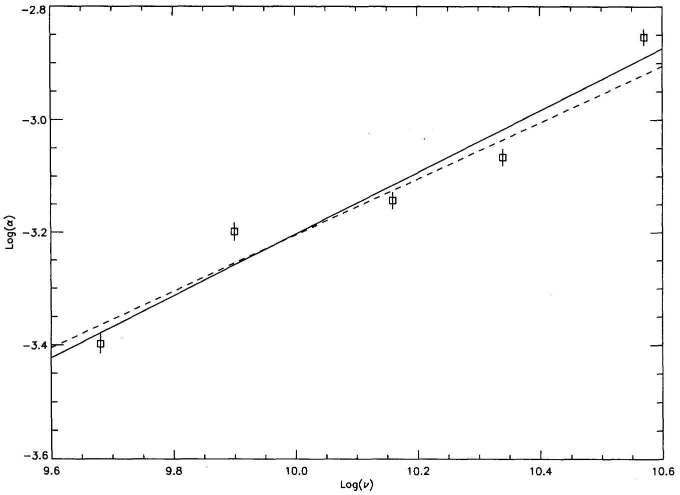

FIG. 9.—The horizontal axis is log ν, and the vertical axis is log α, where α parameterizes the frequency-dependent variability timescale $\tau(\nu) \propto \nu^{-\alpha}$. The model predicts $\alpha = 0.5$, which is depicted by the dashed line. The solid line represents a fit to the data with $\alpha = 0.54$.

to one of the well-sampled spectra, we then try to fit the other nine outburst spectra while adjusting the minimum number of free parameters, effectively reducing the number of unconstrained parameters available to fit each individual spectrum.

Conversion from flux to luminosity was done assuming a Friedmann cosmology with a q_0 of 0.0, a Hubble constant of 100 km s^{-1} Mpc^{-1}, and an emission-line redshift of 0.595. The continuum slope measured in each frequency band was used to transform each spectrum directly to the rest frame of 3C 345. The spectra sp5 and sp8 were chosen for the initial jet model fits because the Compton fluxes (X-ray observations) were available only for those spectra. The angles θ and ϕ are determined by matching the optical and the X-ray flux levels in the models with those of our spectra. The turnover frequency ν_t and flux F_t, the slope in the IR-optical region α_{s1}, and the radio slopes α_{s2} were all constrained by fitting each spectrum. The Lorentz factor of the upper electron cutoff (Γ_u) was chosen so that the break flux and the optically thin flux either fit the entire IR-optical-UV region or fit the IR region while forming a baseline to the optical-UV flux. The parameters described above, along with the electron distribution index (α_e), are the input parameters for the jet models, and the numerical values of each spectrum are listed in rows 1–8 of Table 3. The second panel of Table 3 lists the calculated model parameters. The constants C_1 and C_2 are intermediate results, while K_1 and B_1 are the normalizations for the electron distribution and magnetic field as described previously. The values m and n are the exponents for the magnetic field and particle densities. R_m is the inner radius of the emitting region in parsecs, and δ is the Doppler boost factor. The third panel lists the mass and the accretion rate needed to account for the excess optical-UV flux in each spectrum which exhibited such an excess. The models calculated for each of the spectra are shown in Figure 10. The heavy dots are the data, the solid line represents the jet SSC spectrum, and the dotted line is the accretion disk flux. The turnover frequency was at lower frequencies, and the turnover flux was substantially less in sp1 than in the other spectra. Once the outburst began, the turnover frequency and flux increased and then remained effectively constant at log ν

TABLE 3

MODEL FIT PARAMETERS

PARAMETER	SPECTRUM											
	sp81	sp83	sp1	sp2	sp3	sp4	sp5	sp6	sp7	sp8	sp9	sp10
A. Fitted SSC Jet Parameters[a]												
θ	0.11	0.06	0.14	0.14	0.14	0.14	0.14	0.14	0.14	0.14	0.14	0.14
ϕ	0.05	0.05	0.05	0.05	0.05	0.05	0.05	0.05	0.05	0.05	0.05	0.05
ν_t	11.34	11.75	10.89	10.79	10.83	10.83	10.83	10.83	10.8	10.8	10.8	10.83
F_t	−21.9	−22.1	−22.2	−21.8	−21.8	−21.8	−21.8	−21.8	−21.8	−21.8	−21.8	−21.8
α_e	0.59	0.69	0.59	0.59	0.59	0.59	0.59	0.59	0.59	0.59	0.59	0.59
α_{s1}	0.15	0.26	0.09	−0.39	−0.42	−0.42	−0.39	−0.39	−0.39	−0.39	−0.39	−0.39
α_{s2}	1.25	1.12	1.45	1.45	1.45	1.45	1.45	1.45	1.45	1.45	1.45	1.45
Γ_u	4.1	19	5.3	8.6	8.6	8.6	7.5	8.5	4.3	3.2	3.3	3.3
B. Calculated SCC Jet Parameters[b]												
C_1	1.2	51	1.2	1.2	1.2	1.2	1.2	1.2	1.2	1.2	1.2	1.2
C_2	3.4	1.6	3.4	3.4	3.4	3.4	3.4	3.4	3.4	3.4	3.4	3.4
m	0.87	0.96	0.85	1.12	1.15	1.15	1.12	1.12	1.12	1.12	1.12	1.12
n	2.03	1.77	2.12	2.4	2.42	2.43	2.4	2.4	2.4	2.4	2.4	2.4
K_1	1.33	4.47	1.1	1	1.4	1.37	1.2	1.2	1.2	1.2	1.2	1.2
B_1	0.83	0.56	1.16	2.6	2.4	2.5	2.45	2.45	2.6	2.6	2.6	2.6
R_m	1	0.34	2.72	7.3	6.6	7	6.8	6.8	7.4	6.4	7.4	7.4
δ	6.76	16.52	4.53	4.53	4.53	4.53	4.53	4.53	4.53	4.53	4.53	4.53
C. Fitted Accretion Disk Parameters[c]												
M	4.3	4.3	...	4.5	4.3	4.5	4.3	4.3	...	4.3	4.3	...
$\dot{M}$	3.3	2.2	...	5.0	5.0	6.4	2.0	4.0	...	1.0	4.1	...

[a] θ and ϕ are in radians; Γ is the Lorentz factor $\times 10^{-4}$.

[b] C_1 is in units of 10^{18}, C_2 is the units of 10^{-11}, K_1 is in units of 10^{-4}, R is in parsecs, and B is in gauss.

[c] M is in units of 10^{-9} $M_\odot$, and $\dot{M}$ is in $M_\odot$ yr^{-1}.

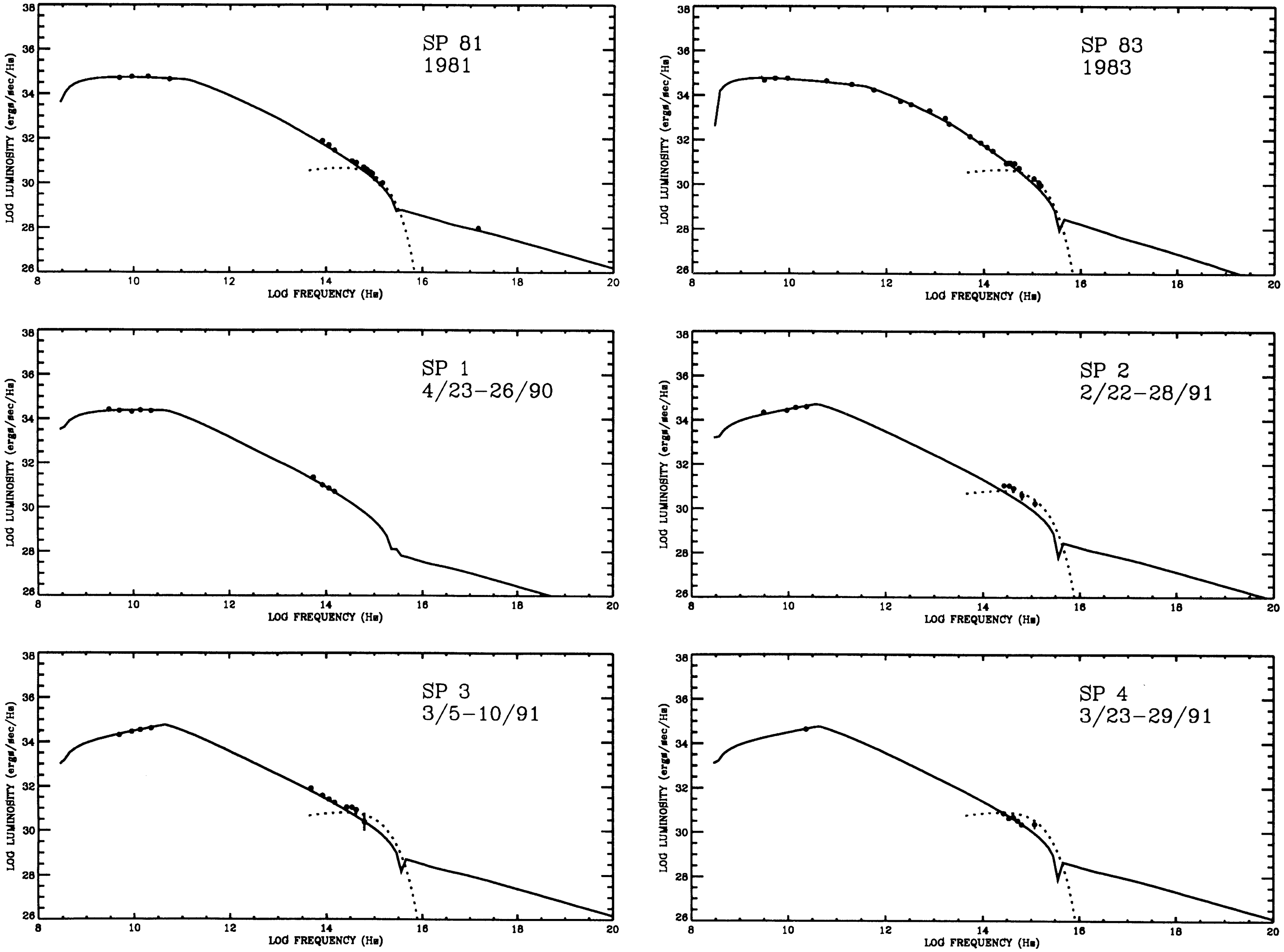

FIG. 10.—Model fits to the multifrequency spectra, including the Bregman et al. (1986) spectra. The heavy dots are data points, the solid line indicates the Königl (1981) SSC model, and the dotted line in the accretion disk component.

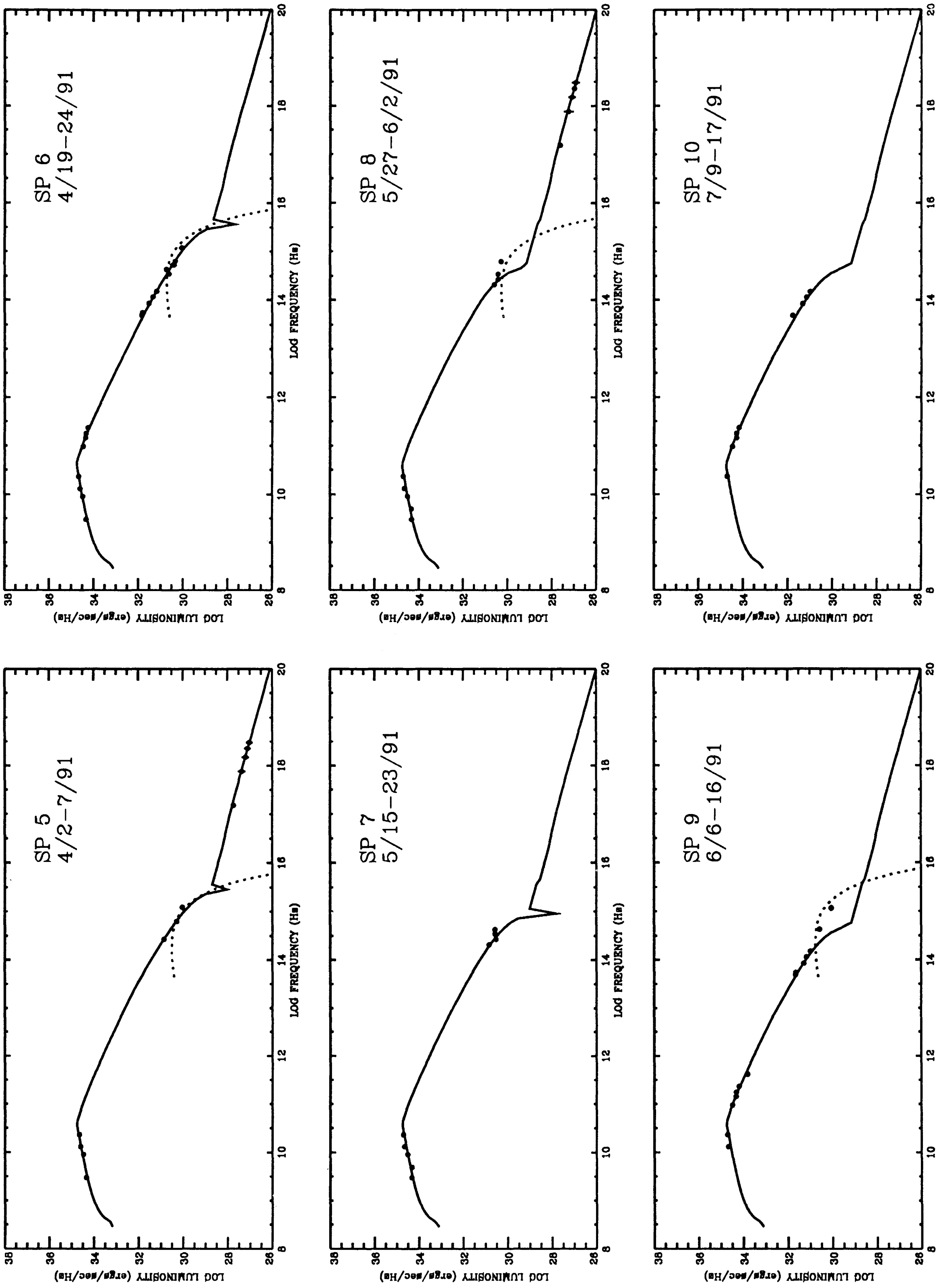

FIG. 10—*Continued*

$= 10.79$ Hz and $\log F = -21.8$ ergs cm^{-2} s^{-1} Hz^{-1}. The only parameter changed in generating jet models for sp2–sp10 was the upper electron cutoff of the injected electron distribution. The value of the upper electron cutoff energy changed from a Lorentz factor of 86,000 to one of 33,000 as the outburst subsided. Calculated values for the magnetic field strength, number density of electrons, and their radial dependencies all remaining fairly constant in the models as the outburst progressed.

3C 345 is among a subclass of blazar AGNs which exhibit the so-called big blue-bump component. In order to study the blue-bump emission, we subtracted the calculated best-fit jet model spectrum from the data to obtain residuals in the blue-UV spectral region. A statistically significant, positive residual is seen for six of seven cases where the blue-UV part of the spectrum is adequately sampled. We then fitted a thermal accretion disk spectrum to these residual spectra. The model involves thermal emission due to viscous dissipation in the steady state accretion disk which has been modified to include the effects of gravitational redshift and focusing (e.g., Sun & Malkan 1989); we have employed computational methods similar to those described in Czerny, Czerny, & Grindlay (1986). A Schwarzschild metric was used in the calculations, and an inclination of $\sin i = 0.5$ was assumed. We fixed the inner disk radius at $3R_g$ and $R_{\rm out}/R_{\rm in} = 10^3$.

Reasonable fits were obtained for several cases—sp2, sp3, sp83, and sp81—with less satisfactory fits in other cases. There is no significant blue-bump excess in sp1, sp7, and sp10, so no fits were attempted. The fits to the multiepoch data were used to interpret the observed variability in the context of physical parameters. Initial fitting was used to estimate an "average" central black hole mass. We then fixed the mass to this value and repeated the fits, interpreting variations in the blue-bump luminosity as a varying accretion rate.

Figure 11 depicts the residual blue-bump luminosity integrated over our fit to the data between $\log \nu = 14.5$–16.5, versus the integrated underlying SSC jet luminosity. The upper two points (*triangles*) are from the Bregman et al. (1986) spectra. If there is any trend at all in our data, it is a slight increase in blue-bump luminosity with increasing SSC luminosity. This suggests that if our interpretation of the blue bump as an accretion disk is correct, the accretion rate varies in the same sense as the SSC jet luminosity. Indeed, it is of interest that an excess is seen at all during outburst, since it is generally assumed that the synchrotron component is the dominant flaring component. We also note that the spectra for which no significant blue bump was seen extend over the full horizontal range of Figure 11. Table 3 lists the estimated parameter values and the calculated values in the context of the SSC jet/disk models. The spectra (including sp81 and sp83) are listed across the top, while the values of the various fitted and calculated parameters identified in column (1) are listed in vertical columns. Table 3A includes parameters constrained by direct model fitting to the data. The calculated physical parameters such as the magnetic field and minimum radius are given in Table 3B. Table 3C gives the mass and accretion rate derived when possible. It should be noted that the 1981 and 1993 fitted and calculated parameters were all very different from those derived for the 1991 flare.

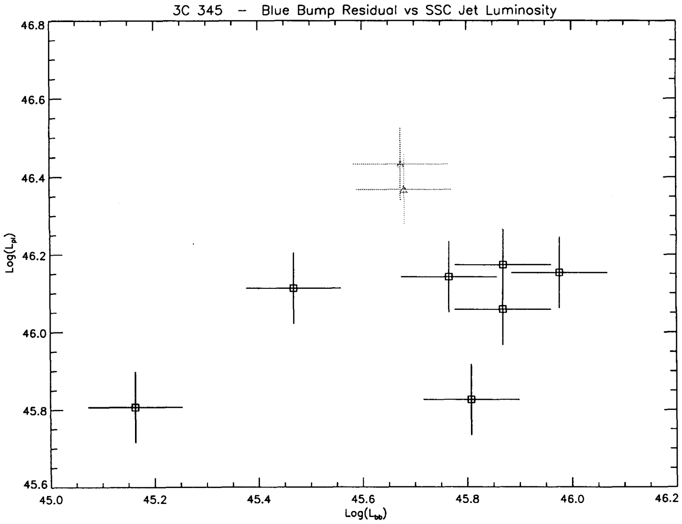

FIG. 11.—"Blue-bump" luminosity vs. the SSC-jet luminosity. A mild correlation exists between the luminosities for the 1991 outburst data. The two upper points are the sp81 and sp83 spectra.

4. CONCLUSIONS

We have undertaken a program to study the multifrequency variability of a blazar during an energetic outburst. From our observations of the 1991 3C 345 outburst, we have constructed 10 nearly simultaneous multifrequency spectra, some of which cover a range of nearly 10 decades in frequency. Comparison of the relationship between frequency and rise time in a simple electron injection model and the rise times seen in the radio flux curves show that the radio data is consistent with the simple injection model. The multifrequency spectral evolution was then modeled in terms of a SSC jet in which the upper cutoff of the relativistic electron distribution changes with time, and an accretion disk in which the accretion rate also varies with time. Modeling several multifrequency spectra of the same source during an outburst allows us effectively to decrease the number of free parameters, which is a common problem with complicated jet models. Comparison of the luminosity in the jet component with that of the blue-bump component shows a marginal linear correlation, suggesting that the accretion rate increases as the jet luminosity increases.

Further separation of the jet and disk components would be expedited by obtaining simultaneous optical polarization measurements during an outburst. Data of this type, with sufficient frequency and temporal sampling, could provide stringent tests of more physical jet models, i.e., those incorporating shocks and using numerical simulations instead of analytical approximations (such as reacceleration).

J. R. W. would like to acknowledge NASA grant NAG 5-1735 and all of the staff at *IUE*. J. R. W. also wishes to thank S. Mufson and D. Hutter for use of and discussions about their jet model code. A. S. would like to thank the staff at Lowell Observatory and Capilla Peak for observing time. A. G. S. would like to acknowledge a long series of grants from the National Science Foundation. H. D. A., M. F. A. and P. A. H. acknowledge support through NSF grant AST 91-20224.

REFERENCES

Aller, H. D., Aller, M. F., Latimer, G. E., & Hodge, P. E. 1985, ApJS, 59, 513

Aller, M. F. 1993, private communication

Bartel, N., Ratner, M. I., Shapiro, I. I., Herring, T. A., & Corey, B. E. 1984, in IAU Symp. 110, VLBI and Compact Radio Sources, ed. R. Fanti, K. Kellermann, & G. Setti (Dordrecht: Reidel), 113

Borgeest, U. & Schramm, J. 1991, IAU Circ., No. 5225

Bregman, J. N., et al. 1986, ApJ, 301, 708

Brown, L. M. J., Robson, E. I., Gear, W. K., & Smith, M. G. 1989, ApJ, 340, 150

Burbidge, E. M. 1965, ApJ, 142, 1674

Crenshaw, D. M., Bruegman, O. W., & Norman, D. J. 1990, PASP, 102, 463

Czerny, B., Czerny, M., & Grindlay, J. E. 1986, ApJ, 311, 241

Duncan, W. D., et al. 1990, MNRAS, 243, 126

Hewitt, A., & Burbidge, G. 1987, ApJS, 63, 1

Hutter, D. J., & Mufson, S. L. 1986, ApJ, 301, 50

Kidger, M. R., de Diego, J. A., Takalo, L. O., Sillanpaa, A., & Okyuda, M. 1993, preprint

Kidger, M., & Takalo, L. 1990, A&A, 239, L9

Königl, A. 1981, ApJ, 243, 700

Kollgaard, R. I., Wardle, J. F. C., & Roberts, D. H. 1989, AJ, 97, 1550

Marscher, A. P., & Gear, W. K. 1985, ApJ, 298, 114

Robson, E. I. 1992, in Variability of Blazars, ed. E. Valtaoja & M. Valtonen (Cambridge: Cambridge Univ. Press), 111

Sadun, A. C. 1992, JRASC, 86, 15

Seaton, M. J. 1979, MNRAS, 187, 73

Smith, P. S., Balonek, T. J., Heckert, P. A., & Elston, R. 1986, ApJ, 305, 484

Smyth, M. J., & Wolstencroft, R. D. 1970, Ap&SS, 8, 471

Sun, W.-H., & Malkan, M. A. 1989, ApJ, 346, 68

Tang, G., Rönnäng, B., & Bååth, L. 1989, A&A, 216, 31

Teräsranta, H., et al. 1992, A&AS, 94, 121

Turner, M. J. L., et al. 1989, PASJ, 41, 345

Urry, C. M. 1984, Ph.D. thesis, Johns Hopkins Univ.

Webb, J. R. 1988, Ph.D. thesis, Univ. Florida

Webb, J. R., Smith, A. G., Leacock, R. J., Fitzgibbons, G. F., Gombola, P. P., & Shepherd, D. W. 1988, AJ, 95, 374